Interior Void Classification in Liquid Metal using Multi-Frequency Magnetic Induction Tomography with a Machine Learning Approach

Imamul Muttakin, *Member, IEEE*, and Manuchehr Soleimani

***Abstract*— Identification of gas bubble, void detection and porosity estimation are important factors in many liquid metal processes. In steel casting, the importance of flow condition and phase distribution in crucial parts, such as submerged entry nozzle (SEN) and mould raises the needs to observe the phenomena. Cross-section of flow shapes can be visualised using the magnetic induction tomography (MIT) technique. However, the inversion procedure in the image reconstruction has either limited resolution or post-processing stages. Additionally, in some cases, the displayed image may not be essential when quantifying the void fraction or porosity. This work proposes an interior void classifier based on multi-frequency mutual induction measurements with eutectic alloy GaInSn as a cold liquid metal model contained in a 3D printed plastic miniature of an SEN. The sensors consist of eight coils arranged in a circle encapsulating the column, providing combinatorial detection on conductive surface and depth. The datasets are induced voltage collections of several non-metallic inclusions (NMI) patterns in liquid metal static test and used to train a machine learning model. The model architectures are a fully connected neural network (FCNN) for 1D; and a convolutional neural network (CNN) for 2D data. The classifier using 1D data has been trained providing 98% accuracy on this dataset. On the other hand, CNN classification using multi-dimensional data produces 96% of test accuracy. Refined with representative flow scenarios, the trained model could be deployed for an intelligent online control system of the liquid metal process.**

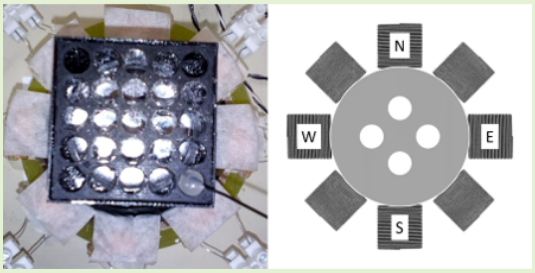

***Index Terms*— Classification, liquid metal, machine learning, magnetic induction tomography, non-metallic inclusion.**

I. Introduction

THE level of void and/or non-metallic inclusions (NMI) needs to be estimated in many liquid metal applications. In continuous steel casting, the presence of NMI, occurring at the primary stage and then more crucial at the casting process (multiphase flow of molten metal and argon gas from tundish to mould), affects the steel cleanliness. Therefore, it is important to observe liquid metal flow shape and structure [1]. Another application that necessitates the observation of porosity of metal in its liquid phase is foam manufacturing [2]. The porosity of the liquid metal will determine the final solid porous metal. Liquid metal is also used for cooling a nuclear reactor [3] [4]. In the liquid metal-cooled reactor, it is desired to detect and characterise the voids due to their influence on heat exchange.

Submitted for review on ... March 2021
This project has received funding from the European Union's Horizon 2020 research and innovation programme under the Marie Skłodowska-Curie grant agreement No 764902.
I. Muttakin is with the Department of Electronic & Electrical Engineering, University of Bath, Claverton Down, BA2 7AY, United Kingdom (e-mail: i.muttakin@bath.ac.uk).
M. Soleimani is with the Department of Electronic & Electrical Engineering, University of Bath, Claverton Down, BA2 7AY, United Kingdom (e-mail: m.soleimani@bath.ac.uk).

Magnetic induction tomography (MIT) system produces mutual induction values as boundary measurements which are then transformed into a cross-sectional image of conductivity distribution. This capability is further enriched by employing frequency-sweep on each measurement resulting in spatio-spectral information. The structure of a conductive body can be explored using the aforementioned spectroscopy [5]. However, spatial resolution is limited especially for recovering small and dispersed interior non-conductive disturbances. Exhaustive algorithm or post-processing is the usual treatments, still, they could not satisfy demands from some industrial applications.

The advancement in artificial intelligence (AI) is accelerated by the availability of data generated from potent sectors. Since the algorithm shows its capability for image interpretation, its implementation progressively finds the broad area of medical, industrial and informatics [6] [7]. This trend also applies in tomography technology [8] [9], where the data and/or the resulting image can be exploited to obtain conclusive outputs. Machine learning (ML) utilised in tomography research has mainly been for the reconstruction scheme [10] [11], image enhancement [12] [13], and various post-processing mechanisms [14] [15]. Those methods are rarely directly targeting primary information embedded in the measurement data. Bypassing the complexity of tomographic image reconstruction, the detection

based on raw data will reduce the computational resources in the deployment phase [16]. Moreover, end-to-end learning of spatio-temporal feature from raw tomography sensor data was assessed to be an efficient scheme [17].

Key parameters in multiphase flow were predicted from multiple sensors reading using a deep-learning method [18]. The model demonstrated generalisation capability for potential field measurement. The work presented in [19] took a direct approach to map the relationship between measurements from electrical capacitance tomography (ECT) sensors and hydrodynamics parameters of flow patterns in a fluidised bed. Although the reconstruction process was still conducted to infer the process parameters, it experimentally collected training samples offline and then the model was used for online monitoring to estimate solid concentration and bubble diameter.

Previously, in cold miniaturised static model experiments, we investigate common two-phase liquid-gas flow scenarios such as full-stream, stratified, bubbly, and annular. These basic flow shapes have been reconstructed with conventional MIT [20]. Accordingly, adaptation of AI become more common in the metallurgy sector [21] [22]. ML approaches for analysing the continuous casting process was surveyed in [23]. Thus, data-driven method and system are prospective for field implementation to extract useful information in helping production. This work attempts to produce a classification of flow inner structure based on multi-frequency mutual induction measurements data.

II. Machine Learning Method using Mutual Induction Data

Among several techniques in employing ML for classification problems reviewed in [24], the following work trains the network from scratch while adjusting an efficient architecture for the given problem and dataset.

For dense layer, where each input feature is assigned a vector of weights that connects to activation output, this operation applies [25]:

$$z^i = W^i x + b^i \tag{1}$$

$$h^i = f^i(z^i) \tag{2}$$

here, W^i and b^i are weights and biases at ith layer respectively. The layer's input is x, and the resulting linear activation z^i is transformed by a non-linear activation function f^i.

There are various activation functions such as sigmoid or hyperbolic tangent. In order to start with the approach based on experimental sensing data, the relatively simpler and faster Rectified Linear Unit (ReLU) will be used.

$$f(z) = max(0, z) \tag{3}$$

On the other hand, convolutional neural network (CNN) conducts:

$$z_n^i = K_n^i * x + b_n^i \tag{4}$$

where n is the index of the feature map, K_n^i is the nth filter kernel, and $*$ is the convolution operator.

In order to reduce the computation cost, the CNN layer is usually accompanied by a pooling layer for sub-sampling the feature map. Max operation finds the maximum value.

The performance is evaluated using accuracy, i.e. ratio of correctly classified samples vs all available samples [22]:

$$acc = \frac{\sum_{m=0}^{k-1} c_{m,m}}{\sum_{m=0}^{k-1} \sum_{n=0}^{k-1} c_{m,n}} \tag{5}$$

where $c_{m,n}$ are the elements of the confusion matrix. The network is also trained to minimise the loss between prediction and true labels.

Mutual induction measurements are conducted using a two-port method with LCR meter and additional switching module (Keysight Technologies) for sequentially selecting a pair out of an 8-coil array at a time. This measurement system has a signal-to-noise ratio (SNR) between 60–90 dB, where measurement at low-frequency opposite-coil has the lowest SNR; and high-frequency adjacent-coil has the highest SNR. The detailed configuration was described in [26]. For the following work (see Fig. 1), all 28 (pair-combination) mutual induction coils are measured and swept from 100 Hz to 100 kHz (logarithmic scale with 28 points).

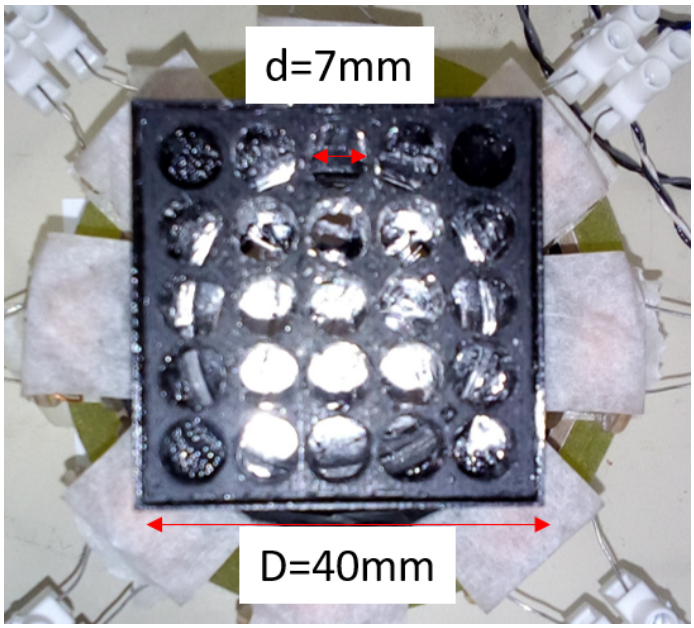

Fig. 1: The liquid metal column with grid for wood inclusion

Pixelated data vector was commonly used as either main or additional input for improving traditional image classification performances [27]. This form of pseudo-image can be built from an array of sensors' reading on the first axis and another measurement dimension on the second axis. An example of a classifier model which is built on limited training images was reported by [28]. Nevertheless, this dataset will be a valuable framework in developing tomographic sensing interpretation using ML [29] [30].

Two methods are investigated: traditional dense fully connected neural network (FCNN) for classifier using one-dimensional (1D) data, and CNN for classifier using two-dimensional (2D) data. Both are implemented in Keras 2.4.0 framework [31] with TensorFlow 2.3.0 backend [32].

III. FCNN Classifier

In the FCNN classifier, the data are built from mutual induction measurement between every coil pair. There are eight coils so that C_2^8 gives 28 data of mutual combination. This is observed at multiple frequency points.

$$\mathbf{M}_{f,n} = \begin{bmatrix} m_{1,1} & \dots & m_{1,28} \\ \vdots & \ddots & \vdots \\ m_{28,1} & \dots & m_{28,28} \end{bmatrix} \tag{6}$$

The measurement data structure in (6) details frequency points f with n mutual induction values. For instance, $m_{1,1}$ is mutual induction between coil-1 and coil-2 at the first frequency point, $m_{1,28}$ is mutual induction between coil-7 and coil-8 at the first frequency point, $m_{28,1}$ is mutual induction between coil-1 and coil-2 at the last frequency point, and $m_{28,28}$ is mutual induction between coil-7 and coil-8 at the last frequency point. Particularly, the phase-shift between the driving signal from transmitting-coil and the detected signal at receiving-coil is taken to represent the sensing information. The measurement is relative values against the reference where liquid metal is full (without any inclusion). θ are phase-shift values for an investigated case, whereas θ_0 are phase-shift values for a reference condition. By this definition, the studied data are 28 $\Delta\theta = \theta - \theta_0$ values at 28 frequency points. The following (7) is applied on each frequency point for all 28 values, where $\mathbf{x}_f$ is $\Delta\theta$ values at frequency f. As a result, a normalised one-dimensional data plot is obtained as shown in Fig. 2. Here, $Index$ 0 corresponds to a data point at f=100 Hz, $Index$ 10 corresponds to a data point at f=2 kHz, and so on.

$$||\mathbf{x}_f|| = \sqrt{\sum_{i=1}^{28} |x_i|^2} \tag{7}$$

A wood (balsa) occupies a single grid in the liquid metal (GaInSn) column. Five classes are studied: 1 wood (central grid), 2 woods (East-West), 3 woods (East-centre-West), 4 woods (North-South East-West), and 5 woods (North-South centre East-West), as shown in Fig. 3. Each case is measured in separate sessions and accompanied by the respective reference measurement. Datasets are created and labelled for five classes, and split into training (80%) and test (20%) data. The validation set is randomly chosen from training data during the training process.

Fig. 4 shows the architecture. Keras model Sequential is constructed consisting of three hidden dense layers, each of which has 128 neurons, with activation function ReLU. Vector of "logits" scores for each class are then converted into probability using a Softmax function. Loss function Sparse Categorical Crossentropy takes a vector of logits and a

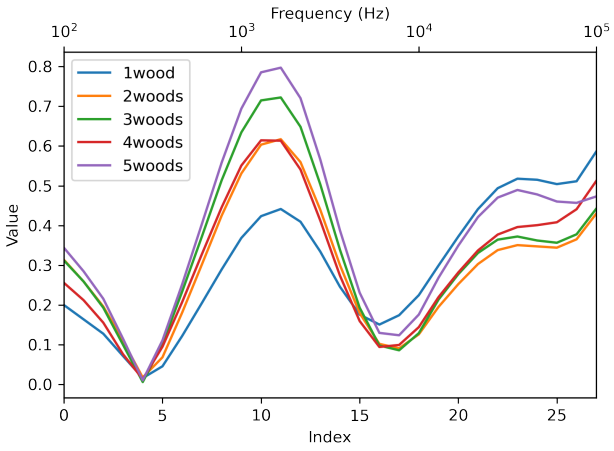

Fig. 2: Norm phase-difference for a number of wood inclusions

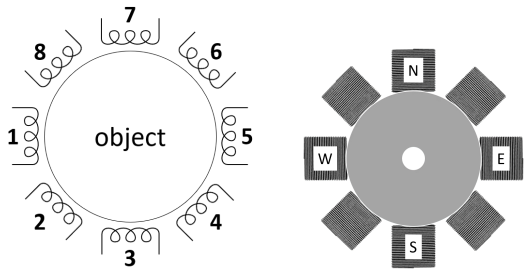

(a) 8-coil MIT sensor

(b) case1

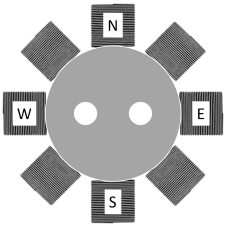

(c) case2

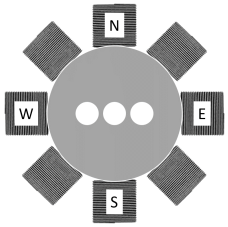

(d) case3

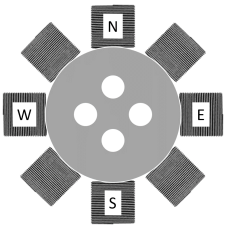

(e) case4

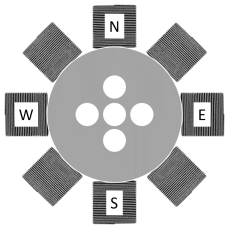

(f) case5

Fig. 3: Wood inclusions in liquid metal cases

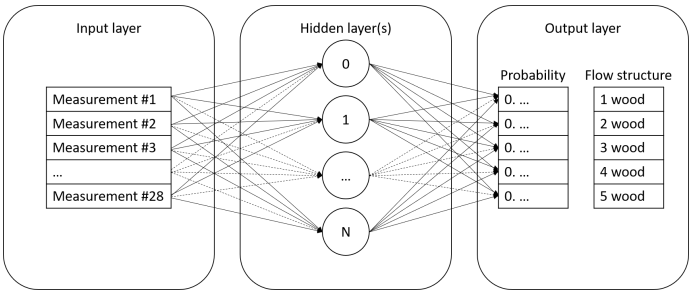

Fig. 4: A neural network with features, hidden layers, and predictions

"True" index and returns a scalar loss for each example. The model is compiled using optimiser ADAptive with Momentum (Adam), utilising "accuracy" metrics to measure the loss and the accuracy of the model. This model will then be fitted adjusting parameters to minimise the loss. The total number of parameters (param) is 53893, all of which are trainable. Model summary is described in Table I.

TABLE I: FCNN Model Summary

Layer	Properties	Output Shape	Param
input	28 x 1	(28)	0
Dense1	Activation: ReLU	(128)	3712
Dense2	Activation: ReLU	(128)	16512
Dense3	Activation: ReLU	(128)	16512
Dense4	Activation: ReLU	(128)	16512
Dense5	+ Softmax	(5)	645

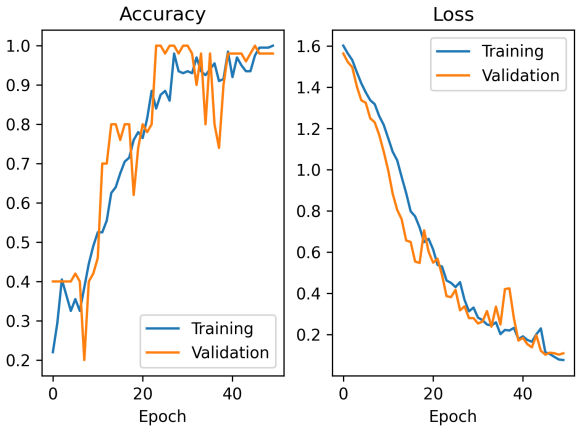

Fig. 5: FCNN training and validation accuracy-loss vs epoch

Fig. 5 shows training and validation accuracy-loss along 50 epochs. At the beginning (1s 36ms/step) train loss is 1.6014, train accuracy is 0.2200, validation loss is 1.5632, and validation accuracy is 0.4000; at the end (0s 8ms/step) train loss is 0.0770, train accuracy is 0.9999, validation loss is 0.1097, and validation accuracy is 0.9800. Performance is checked on validation/test set, giving: test loss 0.11 and test accuracy 0.98. The accuracy on the validation dataset is going lesser than the accuracy on the training dataset starting at epoch>45, indicating overfitting.

Examples of prediction on woods/voids are depicted in Fig. 6. Ten test data are fed into the model, and the prediction bar chart is shown accordingly. The chart shows how confident the model decides that the data corresponds to each class. The confusion matrix is shown in Fig. 7. The map represents tests, where each case has ten predictions. The classifier has a good accuracy, with only four woods case produces a prediction error.

IV. CNN Classifier

Two-dimensional data in the form of multi-frequency phase-difference coil combination are constructed as pseudo-image. The data arrangement follows the structure in (6). This makes a 2D analysis approach is suitable, such as applying a CNN model.

Mutual coil pairs measurements lie on the horizontal axis; whereas frequency points on the vertical axis. Mutual inductance combinations are 28 (from eight coils), so to shape the image into 2D form, the same number of frequency points is set to 28. The measurement frequency is swept in logarithmic fashion from 100 Hz up to 100 kHz. An example of a pseudo-image is shown in Fig 8.

The pseudo-image is 28x28 pixels and the values are scaled between [0 1]. Each value represents $\Delta\theta$ which is a phase-difference measurement of a liquid metal case (θ), against a free-space (air) background reference (θ_0). In addition to cases depicted in Fig. 3, up to nine inclusions are given, and a full liquid metal (no inclusion) condition is incorporated. Therefore, there are ten classes to investigate. Datasets are split into training (80%) and test (20%) data. Validation set is randomly chosen from training data during the training process.

Sequential layers consist of Conv2D, MaxPooling2D, and Dense are stacked for the model, as illustrated in Fig. 9. The diagram gives the information about the input shape, which is a pseudo-image in 2D 28x28 pixels and one 'colour' channel. Subsequent layers are convolution and pooling before the tensor is flattened for the traditional dense neural network. Finally, the last layer provides a number of outputs according to the prediction classes. Table II describes the architecture in detail, where total (trainable) parameters are 93322.

TABLE II: CNN Model Summary

Layer	Properties	Stride	Padding	Output Shape	Param
input	28 x 28 x 1	-	-	(28, 28, 1)	0
Convolution1	Filters: 32 Kernel: 3 x 3 Activation: ReLU	1 x 1	Valid	(26, 26, 32)	320
MaxPooling1	Kernel: 2 x 2	-	Valid	(13, 13, 32)	0
Convolution2	Filters: 64 Kernel: 3 x 3 Activation: ReLU	1 x 1	Valid	(11, 11, 64)	18496
MaxPooling2	Kernel: 2 x 2	-	Valid	(5, 5, 64)	0
Convolution3	Filters: 64 Kernel: 3 x 3 Activation: ReLU	1 x 1	Valid	(3, 3, 64)	36928
Flatten	-	-	-	(576)	0
Dense1	Activation: ReLU	-	-	(64)	36928
Dense2	+ Softmax	-	-	(10)	650

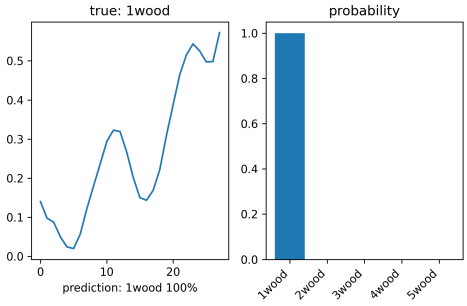

(a) one wood

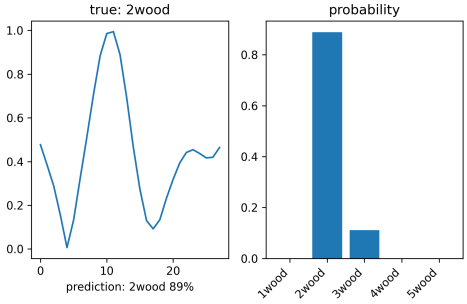

(b) two woods

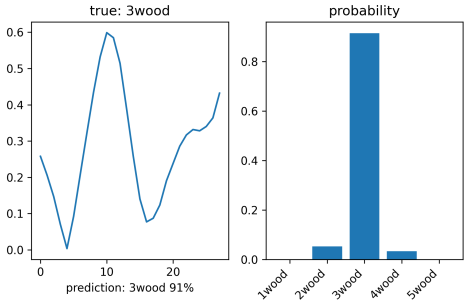

(c) three woods

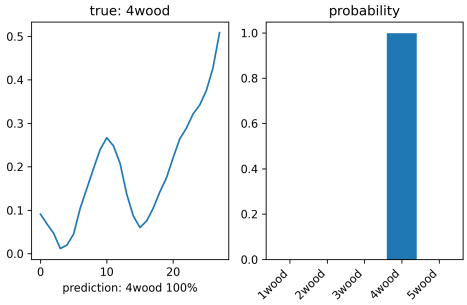

(d) four woods

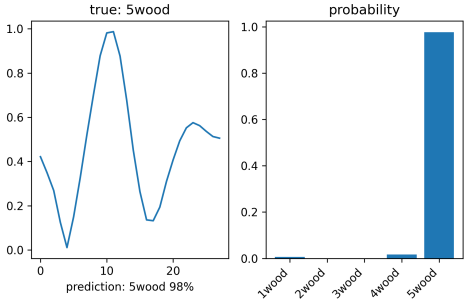

(e) five woods

Fig. 6: Plot prediction of sample case

Fig. 7: FCNN confusion matrix

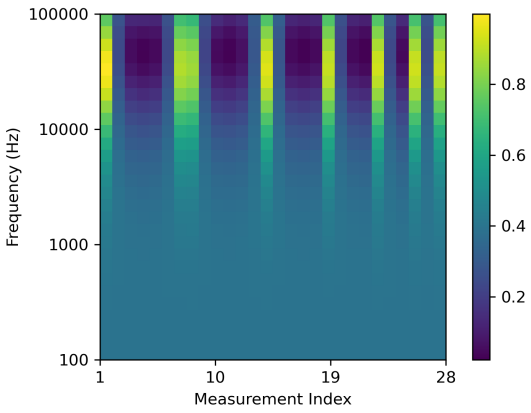

Fig. 8: Pseudo image multi-frequency mutual induction

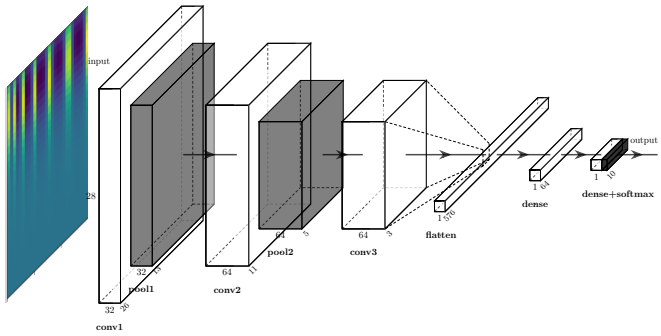

Fig. 9: CNN model

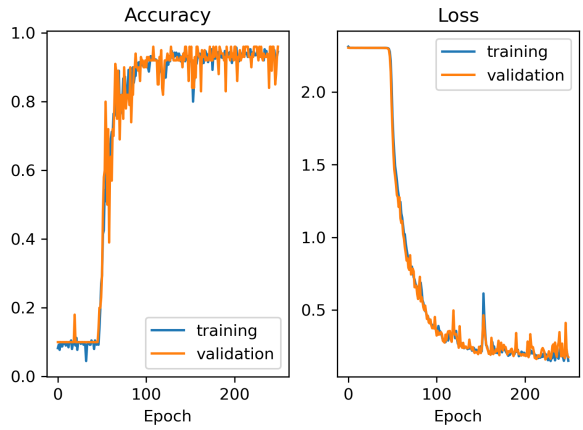

Fig. 10: CNN training and validation accuracy-loss vs epoch

Fig. 10 shows training and validation accuracy-loss along 250 epochs. Performance is checked on validation/test set, giving: test loss 0.18 and test accuracy 0.96. Examples of prediction cases are depicted in Fig 11. Ten test data are fed into the model, and the prediction bar chart is shown accordingly.

The confusion matrix is mapped in Fig. 12. For clarity, the labels associated with inclusion numbers are presented on the axes. Almost all test samples are predicted accurately, except for the full case (no inclusion) where the classifier mispredicts symmetrically distributed of one and five voids/woods (NMI).

V. Discussion

In this study, we define the classification based on the number of voids. It is possible to define the classification in different ways depending on the application. The accuracy of the classifier, on the one hand, depends on the algorithm and training strategies and the other hand depends on the accuracy of the MIT data. With an interest in the interior region of the liquid metal, the accuracy of the MIT setup for low-frequency data will be an important factor.

We intend to provide a prospect of the study for liquid metal processing where void or NMI determination is crucial. The ML approach we develop provides a potent sensing method to address some issues on detecting and characterising the two-phase liquid metal-gas system. Although our case study is for steel-casting where the investigation of bubble distribution in metal flow is desired, this approach would also apply in a wide area of implementation involving liquid metal such as reactor coolant and functional material processing.

For liquid metal fast breeder reactors, real-time radiography is used to image the system [33]. Basic research has been conducted in using neutron radiography for observing liquid metal two-phase flows in vessels. Using the technique reported in [34], radial void fraction profiles were obtained. The follow-up research by authors [35], clarified the basic characteristics of the flow. They visualised the liquid metal two-phase flow and measured its void fraction using neutron radiography and conductivity probe, respectively. The radiography method was

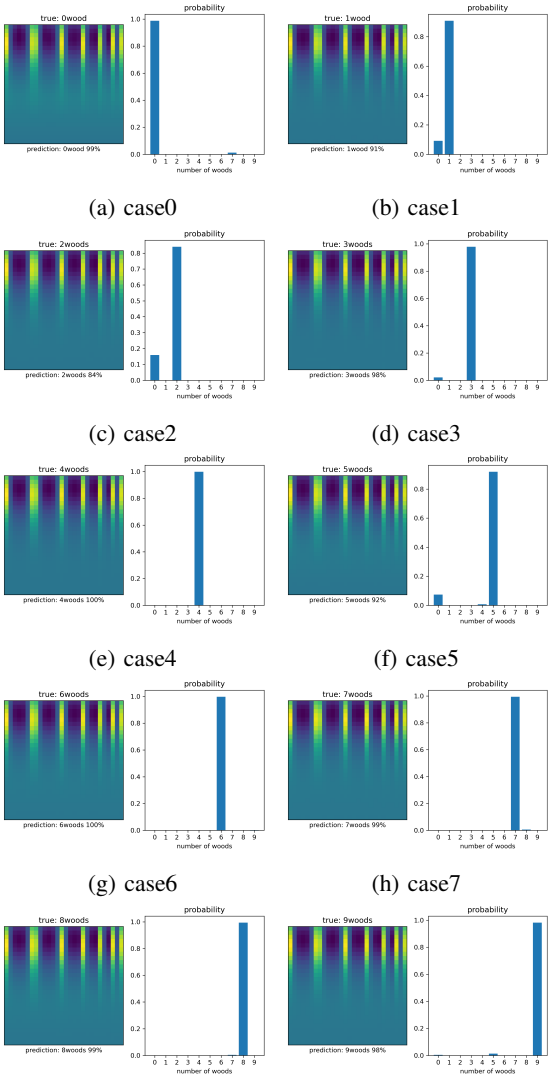

Fig. 11: CNN prediction sample

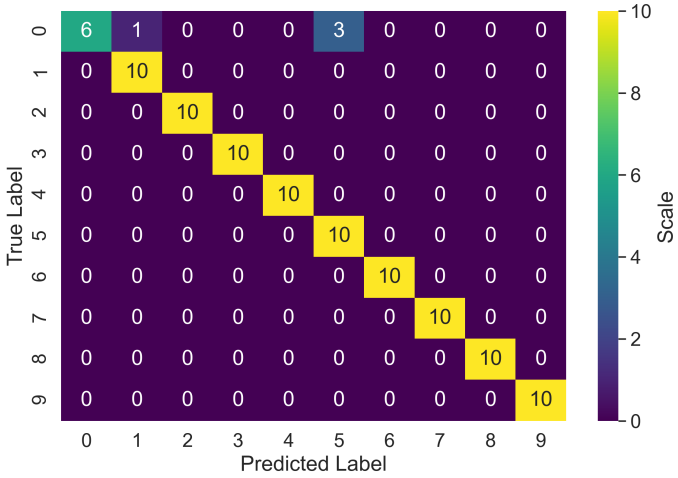

Fig. 12: CNN confusion matrix

used earlier utilising a tracer particle [36]. It requires the attenuation of rays due to the liquid metal being less than $1/e$, and particle size larger than one digitised image element size. The other known method is invasive. A recent technique, optical fibre sensors were used and tested in a well-controlled lab-scale and a pilot-scale reactor [37]. Another report by [38] discloses a probe insertion for detecting gas bubbles in liquid metals.

Porous metal is another engineering material product that is formed in the liquid phase. Its processing method involves bubble generation where pore growth is one of the parameters of interest [39]. Although several modelling methods for liquid metal foam processing have been established [40], experimental observations are still limited. The difficulty in investigating opaque system such as metallic foam is acknowledged. In [41], X-ray tomoscopy was used to clarify the liquid metal's dynamic phenomena, one of which is bubble arrangements.

Generally, alloy casting suffers from inclusions such as dissolved gases. A technique was demonstrated to assess the metal quality by visualising gas content. Albeit only a single dissolved gas in the aluminium alloy was tested by [42]. An online liquid metal cleanliness analyzing system is used for quality assurance of inclusion sensitive products. The commercial system [43] is based on the electric sensing zone.

From the above prior methods, further training data could be gathered to refine our initial model. The simplified experimental data is aimed as a starter to demonstrate the ML approach for liquid metal interior investigation. Additionally, computational fluid dynamics (CFD) simulation would also be used to provide training and validation input. We hope that our proposed method, once escalated to field test could offer an alternative to capture local and quantitative information relevant to operating condition.

VI. Conclusion

The work proposes a liquid metal flow condition classifier focused on the interior voidage. Measurement datasets are multi-frequency mutual induction phase-difference of several wood inclusion variations inside liquid metal GaInSn. The 1D classifier architecture is a multi-layered fully connected neural network (FCNN). After 50 epochs, this model produces a training loss of 0.08, training accuracy 0.99; whereas test accuracy is 98% The 2D classifier architecture is based on a convolutional neural network (CNN). After 250 epochs, this model produces a training loss of 0.15, training accuracy 0.95; whereas test accuracy is 96% The number of woods, or non-metallic inclusions (NMI), classification can be further translated into other quantification such as interior void fraction percentage. This framework provides a prospect for a data-driven liquid metal processing system.

Appendix I
Supplementary Materials

Dataset and script are available upon request: https://github.bath.ac.uk/im463/metal-flow

Acknowledgment

This research made use of the Balena High-Performance Computing (HPC) Service at the University of Bath. The authors would like to thank Dr Thomas Wondrak (HZDR), Ir. Dirk van der Plas, Ir. Sjaak van Oord, and Dr Daniel van Odyck (Tata Steel) for their suggestions on the experiment. David Chapman 's support in measurement setup is also acknowledged. Fig. 9 was visualised using modified version of PlotNeuralNet [44].

References

[1] T. Wondrak, U. Hampel, M. Ratajczak, I. Glavinic, F. Stefani, S. Eckert, D. van der Plas, P. Pennerstorfer, I. Muttakin, M. Soleimani, S. Abouelazayem, J. Hlava, A. Blishchik, and S. Kenjeres, "Real-time control of the mould flow in a model of continuous casting in frame of the TOMOCON project," *IOP Conference Series: Materials Science and Engineering*, vol. 424, p. 012003, oct 2018.

[2] J. Banhart, "Manufacturing routes for metallic foams," *JOM*, vol. 52, no. 12, pp. 22–27, Dec. 2000. [Online]. Available: http://link.springer.com/10.1007/s11837-000-0062-8

[3] P. Planquart, C. Spaccapaniccia, G. Alessi, S. Buckingham, and K. V. Tichelen, "Experimental and numerical characterization of the flow field at the core entrance of a water model of a heavy liquid metal–cooled reactor," *Nuclear Technology*, vol. 206, no. 2, pp. 231–241, 2020. [Online]. Available: https://doi.org/10.1080/00295450.2019.1637240

[4] W. Xu, K.-J. Xu, J.-P. Wu, X.-L. Yu, and X.-X. Yan, "Peak-to-peak standard deviation based bubble detection method in sodium flow with electromagnetic vortex flowmeter," *Review of Scientific Instruments*, vol. 90, no. 6, p. 065105, 2019. [Online]. Available: https://doi.org/10.1063/1.5089690

[5] I. Muttakin and M. Soleimani, "Magnetic induction tomography spectroscopy for structural and functional characterization in metallic materials," *Materials*, vol. 13, no. 11, p. 2639, Jun 2020. [Online]. Available: http://dx.doi.org/10.3390/ma13112639

[6] K. Suzuki, "Overview of deep learning in medical imaging," *Radiological Physics and Technology*, vol. 10, no. 3, pp. 257–273, Sep. 2017. [Online]. Available: http://link.springer.com/10.1007/s12194-017-0406-5

[7] Z. Zhang and E. Sejdić, "Radiological images and machine learning: Trends, perspectives, and prospects," *Computers in Biology and Medicine*, vol. 108, pp. 354–370, 2019. [Online]. Available: https://www.sciencedirect.com/science/article/pii/S0010482519300642

[8] G. Wang, "A perspective on deep imaging," *IEEE Access*, vol. 4, pp. 8914–8924, 2016.

[9] M. Araya-Polo, J. Jennings, A. Adler, and T. Dahlke, "Deep-learning tomography," *The Leading Edge*, vol. 37, no. 1, pp. 58–66, 2018. [Online]. Available: https://doi.org/10.1190/tle37010058.1

[10] G. Wang, J. C. Ye, and B. De Man, "Deep learning for tomographic image reconstruction," *Nature Machine Intelligence*, vol. 2, no. 12, pp. 737–748, Dec. 2020. [Online]. Available: http://www.nature.com/articles/s42256-020-00273-z

[11] Y. Wu, B. Chen, K. Liu, C. Zhu, H. Pan, J. Jia, H. Wu, and J. Yao, "Shape reconstruction with multiphase conductivity for electrical impedance tomography using improved convolutional neural network method," *IEEE Sensors Journal*, pp. 1–1, 2021.

[12] Z. Wei, D. Liu, and X. Chen, "Dominant-current deep learning scheme for electrical impedance tomography," *IEEE Transactions on Biomedical Engineering*, vol. 66, no. 9, pp. 2546–2555, Sep. 2019.

[13] Z. Chen, Q. Yuan, X. Song, C. Chen, D. Zhang, Y. Xiang, R. Liu, and Q. Xuan, "Mitnet: Gan enhanced magnetic induction tomography based on complex cnn," 2021.

[14] J. Yao, H. Chen, Z. Xu, J. Huang, J. Li, J. Jia, and H. Wu, "Development of a wearable electrical impedance tomographic sensor for gesture recognition with machine learning," *IEEE Journal of Biomedical and Health Informatics*, vol. 24, no. 6, pp. 1550–1556, June 2020.

[15] S. Kaji and S. Kida, "Overview of image-to-image translation by use of deep neural networks: denoising, super-resolution, modality conversion, and reconstruction in medical imaging," *Radiological Physics and Technology*, vol. 12, no. 3, pp. 235–248, Sep. 2019. [Online]. Available: http://link.springer.com/10.1007/s12194-019-00520-y

[16] H. Lee, C. Huang, S. Yune, S. H. Tajmir, M. Kim, and S. Do, "Machine Friendly Machine Learning: Interpretation of Computed Tomography Without Image Reconstruction," *Scientific Reports*, vol. 9, no. 1, p. 15540, Dec. 2019. [Online]. Available: http://www.nature.com/articles/s41598-019-51779-5

[17] O. Costilla-Reyes, P. Scully, and K. B. Ozanyan, "Deep neural networks for learning spatio-temporal features from tomography sensors," *IEEE Transactions on Industrial Electronics*, vol. 65, no. 1, pp. 645–653, Jan 2018.

[18] J. Li, D. Hu, W. Chen, Y. Li, M. Zhang, and L. Peng, "Cnn-based volume flow rate prediction of oil–gas–water three-phase intermittent flow from multiple sensors," *Sensors*, vol. 21, no. 4, 2021. [Online]. Available: https://www.mdpi.com/1424-8220/21/4/1245

[19] Q. Guo, M. Ye, W. Yang, and Z. Liu, "A machine learning approach for electrical capacitance tomography measurement of gas–solid fluidized beds," *AIChE Journal*, vol. 65, no. 6, p. e16583, 2019. [Online]. Available: https://aiche.onlinelibrary.wiley.com/doi/abs/10.1002/aic.16583

[20] I. Muttakin, T. Wondrak, and M. Soleimani, "Magnetic induction tomography sensors for quantitative visualization of liquid metal flow shape," *IEEE Sensors Letters*, vol. 4, no. 7, pp. 1–4, July 2020.

[21] I. Mohanty and D. Bhattacherjee, "Artificial Neural Network and Its Application in Steel Industry," in *Computational Approaches to Materials Design: Theoretical and Practical Aspects*, S. Datta and J. P. Davim, Eds. Hershey, PA: IGI Global, 2016, pp. 267–300. [Online]. Available: http://doi:10.4018/978-1-5225-0290-6.ch010

[22] C. Kusche, T. Reclik, M. Freund, T. Al-Samman, U. Kerzel, and S. Korte-Kerzel, "Large-area, high-resolution characterisation and classification of damage mechanisms in dual-phase steel using deep learning," *PLOS ONE*, vol. 14, no. 5, pp. 1–22, 05 2019. [Online]. Available: https://doi.org/10.1371/journal.pone.0216493

[23] D. Cemernek, S. Cemernek, H. Gursch, A. Pandeshwar, T. Leitner, M. Berger, G. Klösch, and R. Kern, "Machine learning in continuous casting of steel: a state-of-the-art survey," *Journal of Intelligent Manufacturing*, Mar. 2021. [Online]. Available: https://doi.org/10.1007/s10845-021-01754-7

[24] H. Shin, H. R. Roth, M. Gao, L. Lu, Z. Xu, I. Nogues, J. Yao, D. Mollura, and R. M. Summers, "Deep convolutional neural networks for computer-aided detection: Cnn architectures, dataset characteristics and transfer learning," *IEEE Transactions on Medical Imaging*, vol. 35, no. 5, pp. 1285–1298, May 2016.

[25] N. Alqahtani, F. Alzubaidi, R. T. Armstrong, P. Swietojanski, and P. Mostaghimi, "Machine learning for predicting properties of porous media from 2d x-ray images," *Journal of Petroleum Science and Engineering*, vol. 184, p. 106514, 2020. [Online]. Available: https://www.sciencedirect.com/science/article/pii/S0920410519309350

[26] I. Muttakin and M. Soleimani, "Noninvasive conductivity and temperature sensing using magnetic induction spectroscopy imaging," *IEEE Transactions on Instrumentation and Measurement*, vol. 70, pp. 1–11, 2021.

[27] S. P. Sotiroudis, P. Sarigiannidis, S. K. Goudos, and K. Siakavara, "Fusing diverse input modalities for path loss prediction: A deep learning approach," *IEEE Access*, vol. 9, pp. 30 441–30 451, 2021.

[28] Y. Li, X. Qin, Z. Zhang, and H. Dong, "A robust identification method for nonferrous metal scraps based on deep learning and superpixel optimization," *Waste Management & Research*, vol. 0, no. 0, p. 0734242X20987884, 2021, pMID: 33499775. [Online]. Available: https://doi.org/10.1177/0734242X20987884

[29] J. Zheng, J. Li, Y. Li, and L. Peng, "A benchmark dataset and deep learning-based image reconstruction for electrical capacitance tomography," *Sensors*, vol. 18, no. 11, 2018. [Online]. Available: https://www.mdpi.com/1424-8220/18/11/3701

[30] N. Vahabi, R. Yerworth, M. Miedema, A. van Kaam, R. Bayford, and A. Demosthenous, "Deep analysis of eit dataset to classify apnea and non-apnea cases in neonatal patients," *IEEE Access*, vol. 9, pp. 25 131–25 139, 2021.

[31] F. Chollet *et al.*, "Keras," https://keras.io, 2015.

[32] M. Abadi, A. Agarwal, P. Barham, E. Brevdo, Z. Chen, C. Citro, G. S. Corrado, A. Davis, J. Dean, M. Devin, S. Ghemawat, I. Goodfellow, A. Harp, G. Irving, M. Isard, Y. Jia, R. Jozefowicz, L. Kaiser, M. Kudlur, J. Levenberg, D. Mané, R. Monga, S. Moore, D. Murray, C. Olah, M. Schuster, J. Shlens, B. Steiner, I. Sutskever, K. Talwar, P. Tucker, V. Vanhoucke, V. Vasudevan, F. Viégas, O. Vinyals, P. Warden, M. Wattenberg, M. Wicke, Y. Yu, and X. Zheng, "TensorFlow: Large-scale machine learning on heterogeneous systems," 2015, software available from tensorflow.org. [Online]. Available: https://www.tensorflow.org/

[33] A. K. Acharya, A. K. Sharma, C. Avinash, S. K. Das, L. Gnanadhas, B. Nashine, and P. Selvaraj, "Investigation of molten fuel coolant interaction phenomena using real time x-ray imaging of simulated woods metal-water system," *Nuclear Engineering and Technology*, vol. 49, no. 7, pp. 1442–1450, 2017. [Online]. Available: https://www.sciencedirect.com/science/article/pii/S1738573317300700

[34] Y. Saito, K. Mishima, Y. Tobita, T. Suzuki, M. Matsubayashi, I. Lim, and J. Cha, "Application of high frame-rate neutron radiography to liquid-metal two-phase flow research," *Nuclear Instruments and Methods in Physics Research Section A: Accelerators, Spectrometers, Detectors and Associated Equipment*, vol. 542, no. 1, pp. 168–174, 2005, proceedings of the Fifth International Topical Meeting on Neutron Radiography. [Online]. Available: https://www.sciencedirect.com/science/article/pii/S016890020500152X

[35] Y. Saito, K. Mishima, Y. Tobita, T. Suzuki, and M. Matsubayashi, "Measurements of liquid–metal two-phase flow by using neutron radiography and electrical conductivity probe," *Experimental Thermal and Fluid Science*, vol. 29, no. 3, pp. 323–330, 2005, third European-Japanese Two-Phase Flow Group Meeting. [Online]. Available: https://www.sciencedirect.com/science/article/pii/S0894177704000676

[36] N. Takenaka, H. Asano, T. Fujii, Y. Motomura, A. Ono, M. Matsubayashi, and A. Tsuruno, "Liquid metal flow measurement by neutron radiography," *Nuclear Instruments and Methods in Physics Research Section A: Accelerators, Spectrometers, Detectors and Associated Equipment*, vol. 377, no. 1, pp. 156–160, 1996, proceedings of the Second International Topical Meeting on Neutron. [Online]. Available: https://www.sciencedirect.com/science/article/pii/0168900296001349

[37] C. Corazza, K. Rosseel, W. Leysen, K. Gladinez, A. Marino, J. Lim, and A. Aerts, "Optical fibre void fraction detection for liquid metal fast neutron reactors," *Experimental Thermal and Fluid Science*, vol. 113, p. 109865, 2020. [Online]. Available: https://www.sciencedirect.com/science/article/pii/S0894177719303681

[38] M. Schneider and J. W. Evans, "A novel probe for detecting gas bubbles in liquid metals," *Metallurgical and Materials Transactions B*, vol. 37, no. 3, pp. 333–337, Jun. 2006. [Online]. Available: https://doi.org/10.1007/s11663-006-0018-7

[39] A. Katayose, R. Yokose, K. Obata, and T. Makuta, "New fabrication method and properties of porous metals produced by ultrasonic control of microbubble size," *Microsystem Technologies*, vol. 24, no. 1, pp. 709–713, Jan. 2018. [Online]. Available: http://link.springer.com/10.1007/s00542-017-3390-0

[40] V. Gergely and T. Clyne, "Drainage in standing liquid metal foams: modelling and experimental observations," *Acta Materialia*, vol. 52, no. 10, pp. 3047–3058, 2004. [Online]. Available: https://www.sciencedirect.com/science/article/pii/S1359645404001417

[41] F. García-Moreno, P. H. Kamm, T. R. Neu, F. Bülk, R. Mokso, C. M. Schlepütz, M. Stampanoni, and J. Banhart, "Using X-ray tomoscopy to explore the dynamics of foaming metal," *Nature Communications*, vol. 10, no. 1, p. 3762, Aug. 2019. [Online]. Available: https://www.nature.com/articles/s41467-019-11521-1

[42] S. Fox and J. Campbell, "Liquid metal quality," *International Journal of Cast Metals Research*, vol. 14, no. 6, pp. 335–340, 2002. [Online]. Available: https://doi.org/10.1080/13640461.2002.11819451

[43] R. I. L. Guthrie and M. Li, "In Situ detection of inclusions in liquid metals: Part I. Mathematical modeling of the behavior of particles traversing the electric sensing zone," *Metallurgical and Materials Transactions B*, vol. 32, no. 6, p. 1067, Dec. 2001. [Online]. Available: https://doi.org/10.1007/s11663-001-0095-6

[44] H. Iqbal, "Harisiqbal88/plotneuralnet v1.0.0," Dec. 2018. [Online]. Available: https://doi.org/10.5281/zenodo.2526396